Kinematic inversion of fault slip during the nucleation of laboratory earthquakes

P. Dublanchet[1], F.X. Passelègue [2], H. Chauris[1], A. Gesret[1], C. Twardzik[2]

[1]Mines Paris, PSL University, Centre for geosciences and geoengineering, 77300 Fontainebleau, France
[2]Géoazur, Université de Côte d'Azur Nice, France

Key Points:

- We design a new kinematic slip inversion method for laboratory faults based on finite elements analysis and strain measurements
- The nucleation of laboratory earthquakes consists of aseismic slip events expanding at speeds between 1 and 100 meters per day
- High resolution imaging of slip in the laboratory requires high density strain gauge arrays evenly distributed around the fault

Corresponding author: Pierre Dublanchet, `pierre.dublanchet@minesparis.psl.eu`

Abstract

Decades of geophysical monitoring have revealed the importance of slow aseismic fault slip in the release of tectonic energy. Although significant progress have been made in imaging aseismic slip on natural faults, many questions remain concerning its physical control. Here we present an attempt to study the dynamics of aseismic slip in the controlled environment of the laboratory. We develop a kinematic inversion method, to image the evolution of slip triggered by a fluid injection within a saw-cut sample loaded in a tri-axial cell. We use the measurements from a strain gauge array placed in the vicinity of the fault, and the observed shortening of the sample, to invert the fault slip distribution in space and time. The inversion approach relies both on a deterministic optimization step followed by a Bayesian analysis, so that uncertainties are quantified. We show that the injection of fluid triggers aseismic slip events that propagate along the fault in a crack-like manner at a speed of the order of 1 to 100 m.day^{-1}, before degenerating into a dynamic rupture. The total amount of aseismic slip accumulated during this nucleation phase reaches 10-30 μm locally. Numerical investigations indicate that with a denser strain gauge array, this method has the potential to reveal the details of aseismic slip propagation in a laboratory sample with unprecedented resolution, which will improve our understanding of earthquake nucleation. The application presented here also reveals important hydro-mechanical aspects of the faults, when our results are confronted to previous estimations of the hydraulic properties.

Plain Language Summary

Major faults situated at tectonic plate boundaries accommodate relative plate motion by a series of earthquakes, where an offset is created in a few seconds to minutes, or by slow slip episodes accumulating the same amount of slip over hours to several days. Slow slip events are of particular interest since they are suspected to play a role in the preparatory phase of damaging earthquakes. Measurements of ground deformation reveal how these events develop on real faults, but the physical control on this process remains elusive. Here we present an attempt to image the development of slow slip events in the controlled context of a laboratory experiment where a centimetric scale fault is activated by a fluid injection, using local deformation measurements. Our study reveals that slow slip events are initiated preferentially in the vicinity of the fluid pressure source, expand along the fault at speeds of the order of 1 to 100 m.day^{-1}, accumulating 10 to 30 μm of relative displacement. We also discuss extensively the resolution of our method, and provide recommendations to optimize the measurements. Our method has the potential to improve significantly the interpretability of rock mechanics experiments.

1 Introduction

Estimating the spatial and temporal evolution of slip along fault interfaces is crucial to understand the physics of deformation phenomena occurring in the crust during the different stages of the seismic cycle (Avouac, 2015). However, because fault slip occurs at depth under extreme environmental conditions, direct in-situ measurements remain nowadays impossible, and these estimates are solely based on inverse problem theory (Ide, 2007). Therefore, our understanding of earthquake physics is limited by the resolution and the density of the data inverted, as well as the complexity of the forward problem (Saraó et al., 1998; Beresnev, 2003; S. Hartzell et al., 2007; Mai et al., 2016).

The forward problem consists of determining the three-dimensional Green's functions of the surrounding medium, which provide estimates of the stress change (Lamb, 1904; L. R. Johnson, 1974) or the wave fields (Bouchon & Aki, 1977; Bouchon, 1981) in the medium with respect to a given fault slip history. Note that in such elastic models, the observed deformations of the medium are expected to be related exclusively to the slip of the fault.

The inverse problem consists of characterizing the spatiotemporal evolution of the rupture process from the recorded motions (seismometer or geodetic displacement measurement). Two main difficulties generally arise: the relationship between data and parameters can be non linear, and the inverse problem has a non-unique solution.

To avoid dealing with the non-linearity of the inverse problem, some inversions are carried out using only static data, which provided a static picture of the slip position on a fault plane, without information on how the slip changed over time (e.g., onset, propagation velocity, and termination). Another approach is to linearize the problem (Olson & Apsel, 1982; S. H. Hartzell & Heaton, 1983), allowing the retrieval of the spatial and temporal evolution of slip. However, such approach requires to make strong assumptions regarding the temporal evolution of the rupture front (e.g., fix the rupture front, fix the rise time of the source time function). But, recent advances have been made in nonlinear inversion techniques that allow retrieval of the full kinematic slip history (Ji et al., 2002; Peyrat & Olsen, 2004; Cirella et al., 2009).

These approaches have allowed to unravel some interesting properties about how faults slip. For example, seismological and geodetic inversions have shown that (i) the nature of slip along a fault appears to be spatially and temporally variable (K. M. Johnson et al., 2012), (ii) a slow slip event can develop as a slip dislocation pulse, characterized by a symmetric ramp function (Radiguet et al., 2011a), (iii) the preparation phase of earthquakes can be a mix of seismic and aseismic processes (Twardzik et al., 2022), (iv) large seismic ruptures exhibit complexities, such as segmented ruptures during propagation or later reverse propagation (Gallovič & Zahradník, 2012; Vallée et al., 2023).

Despite these major advances in geophysics, attempts to apply these inverse methods to experimental data sets remain limited. Recent technical advances in experimental rock mechanics make it possible to reproduce the various stages of the seismic cycle in a high-pressure environment while monitoring the evolution of strain in the bulk of the sample (Goto et al., 1991), as well as the pore pressure (Almakari et al., 2020). Almakari et al. (2020) have for instance used pore pressure measurements to invert for fault's hydraulic diffusivity enhancement with injection-induced fault slip in a saw cut sample loaded in a tri-axial cell. However, they did not consider the mechanical data (strain) in their inversion. Strain gauges are commonly used to evaluate the sample mechanical response during rock deformation experiments, the elastic properties of the rock sample and the deviations from elasticity in the final stage of the experiment to macroscopic failure (Lockner et al., 1992). In addition, such strain gauges can also be used to track the change in strain during the development of the slip front (Passelègue et al., 2019, 2020) as well as during the propagation of the dynamic fracture (Passelègue et al., 2016). Here we argue that these measurements, performed under known conditions and near the fault plane, could also be used to invert the spatial and temporal evolution of slip during different stages of laboratory experiments.

In this paper, we make this attempt and invert the evolution of the fault slip during the nucleation phase of laboratory earthquakes. We first computed the Green's function of the fault system using the finite element method and used these functions to invert the fault slip resulting from the spontaneous nucleation of instabilities along the experimental fault. For that we use a specific parametrization to reduce the non-uniqueness of the problem, as suggested by previous studies focusing of real faults. We show that the inversion of the experimental data highlights the growth of a slip patch along the fault during the nucleation of laboratory earthquakes. This new method opens the doors to fault slip imagery at the laboratory scale, allowing (i) a better description of the transient phenomena during the seismic cycle in the laboratory and (ii) the verification of the resolution of inversion methods developed for natural earthquakes on experimental data sets obtained in a controlled and known environment.

2 Dataset: aseismic nucleation of laboratory earthquakes

We consider here the injection experiments presented in Almakari et al. (2020) and Passelègue et al. (2020). In this section, we provide a short summary of the experimental setup and results. The reader can refer to Almakari et al. (2020) for a more detailed description.

A cylindrical saw-cut andesite sample (Figure 1a) was first loaded in a tri-axial cell by increasing the axial load at 90 % of peak strength of the fault. The characteristics of the rock sample used are listed in table 1. Then fluid was injected continuously up to the complete release of the elastic energy stored in the system. The injection was performed through a borehole located at the edge of the fault (Figure 1a), assuming a constant volumetric injection rate of 50 mL/minute. During the whole loading and injection process, the shortening of the sample was monitored, allowing to estimate the average fault slip by projection (red curve in Figure 1b). An array of strain gauges (S1 to S6) also measured the evolution of local strain (Figure 1b). Strain gauges were distributed along the fault (Figure 1a), at 5 mm from it, and measured preferentially the strain (Figure 1c) in the direction of the principal stress σ_1, as presented in Figure 1a. Note that in Figure 1b, we represent the stress time series instead of the the strain, to highlight the overall stress release during the injection experiment. The stress was obtained from the strain measurements, assuming plane-strain deformation of the gauges. The pore pressure at the injection borehole was also monitored (Figure 1b).

The increase of fluid pressure and its associated diffusion induced a complicated sequence of seismicity, which initiated with the propagation of dynamic events, and followed by slow rupture phenomena and finally by stable slip, as described in previous study (Passelègue et al., 2020). A total of three stick-slip events spontaneously nucleated during the fluid injection (red stars in Figure 1b). These three stick slip events were preceded by a nucleation phase, characterized on the strain measurements by a deviation from elasticity, suggesting that inelastic processes occur along the fault before the mainshock. The nucleation phases are highlighted in Figure 1b by the red patches labeled Evt1, Evt2 and Evt3 respectively. In the following sections, we design a method to invert the fault slip history during these three nucleation periods.

3 Method: kinematic slip inversion for stick-slip experiments

The setup we intend to model in this study is a typical rock-mechanics setup consisting of a cylindrical saw-cut rock sample loaded in a tri-axial cell (Figure 1c). The rock sample is modeled as an elastic cylinder of height $h = 8.8$ cm, radius $a = 2$ cm, under confining pressure $\sigma_3 = P_c$ and axial load σ_1 (Figure 1c). The Young's modulus is noted E and the Poisson ratio ν. The sample is saw cut at angle θ with the (vertical) axial load, creating an elliptical fault Σ. We use the Cartesian coordinate system shown in Figure 1c. As the load increases, slip Δu is initiated on the fault. It is defined as the displacement discontinuity across the fault plane Σ:

$$\Delta\vec{u}(\vec{x} \in \Sigma, t) = \vec{u}(\vec{x} \in \Sigma^+, t) - \vec{u}(\vec{x} \in \Sigma^-, t), \tag{1}$$

where $\vec{u}$ is the displacement field, $\vec{x}$ the position and t time. Because of the geometry of the sample and the loading device, we assume that slip only occurs within the fault plane (no opening), in the direction of the great axis of the ellipse (no $\vec{e}_2$ component), so that:

$$\vec{\Delta u}(\vec{x}, t) = \Delta u(\vec{x}, t)\vec{s} = \Delta u(\vec{x}, t)\left[\sin\theta\vec{e}_1 - \cos\theta\vec{e}_3\right]. \tag{2}$$

As mentioned in the previous section, 6 strain gauges are distributed along the fault (Figures 1a and 1c) and continuously measure the strain component ε_{33} related to fault reactivation. Displacement sensors allow to monitor the sample shortening, that can be used to estimate the average fault slip history. Here we derive a method to image the slip evolution on the fault from the strain and average slip measurements, relying on a Green's function approach. For that we consider the static equilibrium of the top-half sample (i.e. the part of the sample situated above the fault). In this domain, delimited by the surfaces S_t, S_l and Σ (Figure 1c), the stress components satisfy:

$$\sigma_{ij,j} = 0. \tag{3}$$

The rock being elastic, the stress components σ_{ij} are related to the strain components ε_{ij} with the Hooke's law:

$$\sigma_{ij} = \frac{E\nu}{(1+\nu)(1-2\nu)}\delta_{ij}\varepsilon_{kk} + \frac{E}{(1+\nu)}\varepsilon_{ij}. \tag{4}$$

The strain components relate to the displacement components as:

$$\varepsilon_{ij} = \frac{1}{2}\left(u_{i,j} + u_{j,i}\right). \tag{5}$$

We also assume the following boundary conditions, guided by the experimental setup:

$$\left\{\begin{array}{lll} \vec{u} & = & \vec{0} \quad \text{on} \quad \vec{x} \in S_t \\ \vec{T} & = & -P_c\vec{e}_r \quad \text{on} \quad \vec{x} \in S_l \\ \vec{u} & = & \frac{1}{2}\Delta u\vec{s} \quad \text{on} \quad \vec{x} \in \Sigma. \end{array}\right. \tag{6}$$

where $\vec{T}$ is the traction on the lateral boundary of the domain. The sample is fixed at the top (no displacement), undergoes a constant confining pressure P_c on the lateral boundary. Slip Δu is prescribed on the fault in the direction $\vec{s}$. To compute the Green's functions necessary for our problem, we prescribe the following unit slip distribution on the fault:

$$\Delta u = \delta_D(\vec{x} - \vec{\xi}), \tag{7}$$

where δ_D is the Dirac delta function. The Green's function $G(\vec{\xi}, \vec{x})$ is then obtained as the ε_{33} component of the strain tensor satisfying (3), assuming (4), (5), (6) and (7). We have:

$$G(\vec{\xi}, \vec{x}) = \varepsilon_{33}(\vec{x}). \tag{8}$$

By superposition, the strain ε_{33} for a general distribution of slip Δu along the fault is then given by:

$$\varepsilon_{33}(\vec{x}, t) = \int_{\Sigma} G(\vec{\xi}, \vec{x})\Delta u(\vec{\xi}, t) d^2\vec{\xi}. \tag{9}$$

The average slip Δu_m writes:

$$\Delta u_m(t) = \frac{1}{\Sigma}\int_{\Sigma} \Delta u(\vec{x}, t) d^2\vec{x}. \tag{10}$$

Equations (9) and (10) are our forward problem, relating the slip distribution (Δu) to the observables ε_{33} and Δu_m. Note that the forward problem is linear as long as the parameters considered are the values of Δu at a specific position $\vec{x}$ and time t. As shown later, we will however use a different parametrization making the inverse problem non-linear.

The forward problem is solved with a finite element approach. We discretize the domain Ω into $N_e = 2582$ linear tetrahedral elements, and the fault surface into $N_f =$

270 linear triangular elements, leading to a typical spacing between nodes of 0.5 cm. The number of nodes along the fault is $N = 157$. We then compute the Green's functions $G(\vec{\xi}, \vec{x})$ by solving the static equilibrium problem, for positions $\vec{\xi}$ corresponding to each N_f node of the fault. These Green's functions are finally evaluated at the N_j positions $\vec{x}_g$ of the strain gauges, and stored in a $(N_j \times N_f)$ matrix $\mathbf{G}$. We have:

$$\mathbf{G}_{ij} = G(\vec{\xi}_j, \vec{x}_{gi}), \quad i = 1, ..., N_j \quad j = 1, ..., N_f. \tag{11}$$

The strains ε_{33} at positions $\vec{x}_g$ and the slip Δu at the fault nodes are also stored into a $N_g \times 1$ vector $\mathbf{S}$, and a $N_f \times 1$ vector $\mathbf{U}$ respectively. Thus, equation (9) becomes:

$$\mathbf{S}(t) = \mathbf{G}\mathbf{U}(t). \tag{12}$$

Similarly, equation (10) could be written as:

$$U_m(t) = \mathbf{M}^T\mathbf{U}(t), \tag{13}$$

where $U_m(t)$ is the value of average slip at time t, the vector $\mathbf{M}$ $(N_f{\times}1)$ is the spatial average operator, and T denotes the transpose. Imaging the fault slip evolution $\Delta u(\vec{x}, t)$ thus reduces to infer $N_f{\times}N_t$ parameters, where N_t is the total number of strain measurements on one strain gauge, or the number of time steps considered. The number of observations is $(N_g{+}1){\times}N_t$. Since $N_g < N_f$, the problem is largely under-determined. In order to reduce the number of unknown parameters, we follow the parametrization proposed by Liu et al. (2006) for the kinematic coseismic slip inversion of the 2004 Parkfield earthquake. Namely, the slip history at node j (U_j) is parametrized as:

$$U_j(t) = \begin{cases} 0 \quad \text{if } t < t_{0j} \\ \frac{1}{2}\Delta u_j \left[1 - \cos\frac{\pi(t-t_{0j})}{T_j}\right] \quad \text{if } t_{0j} < t < t_{0j} + T_j \\ \Delta u_j \quad \text{if } t > t_{0j} + T_j \end{cases} \tag{14}$$

From equation (14), the fault slip at node j is identically zero before an arrival (onset) time t_{0j}, then reaches a maximum value Δu_j over the rise time T_j. After that, it remains constant at Δu_j. The cosine function used here implies a smooth transition from zero slip to Δu_j. Doing so, we reduce the number of unknown parameters from $N_t{\times}N_f$ to $3N_f$. We therefore define a $(3N_f \times 1)$ parameter vector $\mathbf{X}$ as:

$$X_k = \begin{cases} \Delta u_k \quad \text{if } k = 1, ..., N_f \\ t_{0k} \quad \text{if } k = N_f + 1, ..., 2N_f \\ T_k \quad \text{if } k = 2N_f + 1, ..., 3N_f \end{cases} \tag{15}$$

To reduce further the number of parameters to be inverted, we use two meshes: one for the modeling and one for the imaging part. A coarser mesh for the inversion is assumed than the one used to compute the Green's functions. Instead of using $N_f = 157$ nodes, we evaluate $\mathbf{X}$ at the $N_f = 21$ nodes of a new fault mesh composed of triangular elements. To do so, the Green's functions calculated on the finer mesh are interpolated to get the matrix $\mathbf{G}$ for the coarser mesh. The inverse problem then consists of finding $\mathbf{X}$ minimizing the objective function J defined as:

$$\begin{aligned} J(\mathbf{X}) \quad = \quad & \frac{1}{2}\sum_k \left[\mathbf{S_0}(t_k) - \mathbf{G}\mathbf{U}(t_k, \mathbf{X})\right]^T \mathbf{C_{ds}}^{-1} \left[\mathbf{S_0}(t_k) - \mathbf{G}\mathbf{U}(t_k, \mathbf{X})\right] \\ & + \frac{1}{2}\sum_k \left[U_{m0}(t_k) - \mathbf{M^T}\mathbf{U}(t_k, \mathbf{X})\right]^T C_{du}^{-1} \left[U_{m0}(t_k) - \mathbf{M^T}\mathbf{U}(t_k, \mathbf{X})\right] \\ & + \lambda \left(\nabla\mathbf{X}\right)^t \left(\nabla\mathbf{X}\right), \end{aligned} \tag{16}$$

Sample height (RP) h	8.8 cm
Sample section radius (RP) a	2 cm
Fault angle θ w.r.t principal stress (RP)	30°
Young's modulus (RP) E	64 GPa
Poisson ratio (RP) ν	0.23
Confining pressure (RP) P_c	95 MPa
Number of elements for Green's function computation (MP) N_e	2582
Number of nodes on the fault for Green's function computation (MP) N_f^0	157
Number of nodes on the fault for inversion (IP) N_f	21
Standard deviation of strain measurements (IP)	10^{-6}
Standard deviation of mean slip measurements (IP)	0.1 μm
Regularization parameter (IP)λ	10^{-6}-10^{2}

Table 1. Rock sample properties (RP), mesh properties (MP) and inversion parameters (IP).

where $\mathbf{S_0}(t_k)$ is a $(N_g \times 1)$ vector containing the values of ε_{33} at the gauges positions and time t_k, $U_{m0}(t_k)$ the observed mean slip on the fault at time t_k, and λ a regularization parameter. The regularization here consists of minimizing the gradient norm of the parameters $\mathbf{X}$, to favor smoothly varying parameters with position along the fault. $\mathbf{C_{ds}}$ is the $(N_g \times N_g)$ covariance matrix for the strain data. We only consider for $\mathbf{C_{ds}}$ a diagonal matrix to represent the variances of the observed strains, ignoring the crossing terms. C_{du} is the variance of the observed mean slip. The standard deviation of the strain measurements is less than 10^{-6}, and 0.1μm for the mean slip. In order to account for the limitations of the forward model (quasi static approximation, fully rigid boundary condition on the top boundary of the sample), we double these values to calculate the covariance matrices, so that the diagonal components of C_{ds} are $(2.10^{-6})^2$, and $C_{du} = (0.2)^2(\mu m)^2$. We also normalized the strain and slip measurements ($\mathbf{S_0}$ and U_{m0}) by the maximum magnitude of all the strain time series and the mean slip time series, noted ε_0 and u_0 respectively. Accordingly, the slip vector $\mathbf{U}$ is normalized by u_0, and each row of the matrix $\mathbf{G}$ by ε_0/u_0. Time was also normalized by the duration of the measurement time series t_{max}, so that our parameter vector $\mathbf{X}$ was normalized using u_0 and t_{max}. Accordingly, we normalized C_{du} and each component of $\mathbf{C_{ds}}$ by u_0^2 and ε_0^2.

The optimization of the objective function is performed with a BFGS (Quasi-Newton-Broyden Fletcher-Goldfarb-Shanno) algorithm (Broyden, 1970; Fletcher, 1970; Goldfarb, 1970; Shanno, 1970; Fletcher, 1982). The optimization step results in a first estimation of the best model of fault slip. In order to estimate the uncertainty on the fault slip distribution, we conduct in a second step a probabilistic inversion. For that we use the outcome of the first inversion step as an initial model in a Metropolis-Hasting algorithm (application of the Markov Chain Monte Carlo (MCMC) methods (Metropolis et al., 1953; Hastings, 1970)), allowing to sample the posterior distribution of the model parameters $\mathbf{X}$.

In the next sections, we perform a resolution analysis of our inverse problem, and discuss a synthetic test to evaluate the performance of the deterministic part of the kinematic inversion method. Then we present the application to the experiment described in the previous section and Figures 1a. In both sections, we consider the same rock material: the andesite sample characterized by the properties listed in table 1. Table 1 also summarizes the computational parameters used in the following.

4 Resolution analysis

As illustrated in Figure 1a and c, the strain gauge array used in the experiments is located on one side of the fault, so that we have to deal with unevenly distributed measurements. Since the stress (and thus strain) field associated with a growing crack decreases as an inverse power of the distance to the crack tip (BRIAN, 1993), we expect strain gauges to be not sensitive to slip occurring on the other side of the sample fault. To quantify this, we calculate the resolution matrix $\mathbf{R}$ for our problem (Tarantola, 2005) as follows:

$$\mathbf{R} = \mathbf{G}^T \mathbf{C}_{ds}^{-1} \mathbf{G} + C_{du}^{-1} \mathbf{M}\mathbf{M}^T. \tag{17}$$

The normalized diagonal elements r_i of $\mathbf{R}$ are represented in Figure 2a. It clearly indicates that fault regions situated at more than one cm away from the gauges are poorly resolved, and thus if slip occurs it may not be correctly mapped to these parts of the fault (Radiguet et al., 2011b; Twardzik et al., 2021). Note also that three nodes approximately situated at $(-3, -1.2)$, $(0, -2)$ and $(3, -1.2)$ dominate the resolution (r_i is about two times larger there than elsewhere on the fault), essentially because these nodes are very close to a strain gauge. In the following, we define the resolved zone as the nodes i where $r_i >$ 0.01 (below the heavy red dashed line in Figure 2).

An important issue for the application presented in the next section, is the reliability of inverted slip in the region close to the injection borehole (magenta star in Figure 2a). Therefore, we show in Figures 2b, c and d the restitution $\rho_{inj,1}$, $\rho_{inj,2}$ and $\rho_{inj,3}$ of three nodes located close to the injection point. The restitution $\rho_{inj,i}$ corresponds here to the i^{th} line of the resolution matrix R, and indicates to what extent slip on the i^{th} node might be wrongly assigned to other nodes on the fault (Radiguet et al., 2011b; Twardzik et al., 2021). For the two nodes situated in the resolved region of the fault (Figures 2c and d), the restitution is maximum at the node concerned, even if restitution is somewhat leaking on the closest nodes. However, for the node situated in the low resolution domain, (Figure 2b), restitution is maximum at nodes closer to the strain gauges, indicating that slip in the top part of the fault (roughly $x_2 > 0$) can be wrongly assigned in the best resolved fault zone.

The resolution analysis discussed here motivates the use of a regularization (smoothing) term in the definition of the objective function (16), that can limit the effects of poor resolution and restitution.

5 Synthetic test with crack propagation and resolution analysis

We next generate synthetic data using the Green's functions $\mathbf{G}$ from a slip distribution $\Delta u(\vec{x}, t)$ corresponding to an elliptical crack of aspect ratio α growing from the fault center with constant rupture speed v_r and stress drop $\Delta\tau$. The slip distribution is given by:

$$\Delta u(\vec{x}, t) = \begin{cases} \frac{\Delta\tau}{\mu} \sqrt{v_r^2 t^2 - x_1^2 - (\alpha x_2)^2} & \text{if } x_1^2 + \alpha^2 x_2^2 < v_r^2 t^2 \\ 0, & \text{if } x_1^2 + \alpha^2 x_2^2 \geq v_r^2 t^2 \end{cases} \tag{18}$$

where x_1 and x_2 are the coordinates within the fault plane (Figure 1)a, and $\mu = E/2(1+\nu)$ the shear modulus. In these tests, $\alpha = 2$, which is the aspect ratio of the experimental fault. We considered $v_r = 4\times10^{-4}$ m.s^{-1}, so that the crack front reaches the edges of the fault after t_{max} = 100 s, and a stress drop $\Delta\tau$ = 2.6 MPa. The other parameters used are listed in table 1. The strain component ε_{33} and the spatial average of slip are used as data $\mathbf{S_0}$ and U_{m0} in our inversion procedure. We start from an initial model where Δu, t_0 and T are constant on the fault.

Then, we perform the inversion of the synthetic data for different virtual observational networks involving between $N_g = 10$ and $N_g = 61$ strain gauges. We also consider a case with the gauges distribution used for the real experiment of the next section ($N_g = 6$), all situated on one side of the outer ream of the sample (Figure 2). We thus test gauges networks with N_g varying between $0.28N_f$ and $3N_f$. For each gauge distribution, we also considered 9 different values of the regularization parameter λ ranging from 10^{-6} to 10^2. The inverted slip distribution, and the comparison between strain data and inverted model predictions are shown in Figures 3, 4 and 5. In these Figures, we present the results obtained with $\lambda = 10^{-1}$.

For a dense distribution of strain gauges ($N_g \geq N_f$), the slip distribution is generally reasonably well retrieved (Figure 3 second and third rows, Figure 4), with a satisfactory fit between the synthetic strain data and the simulated strain (Figure 5). The propagation of a slip front from the center of the fault is clearly identifiable. As the strain gauges distribution becomes sparser ($N_g = 6$ for instance), the inversion procedure has more difficulties in retrieving the synthetic model (fourth row in Figure 3, Figure 4), although the synthetic strain data are reasonable well reproduced (third row in Figure 5). The growing elliptical patch is retrieved essentially in the well resolved area of the fault ($t = 50$ and $t = 75$s), but in addition, two large slip patches appear on the left end of the fault and in the low resolution area from $t = 50$s. At the end of the test ($t = 100$s) the slip distribution is more elongated along x_1 than in the original model, but with a maximum slip slightly underestimated (Figure 4). From the restitution analysis performed in the previous section, the inversion possibly assigns large slip here to compensate the lack of slip in the poorly resolved region (top left zone in the last panel of Figure 3), so that the observed average slip on the fault is reproduced.

Note that the high frequency component of strain changes is not well retrieved by the inversion, even for a dense strain gauge array (Figure 5). In particular, the abrupt change and peak in strain associated with the crack front are not retrieved. We attribute this to the parametrization used for the inversion, implying a smooth cosine function. However, as shown later, the experimental data used do not exhibit such rapid variation of strain, so that our parametrization should not affect the quality of the data fitting.

In order to further quantify the performance of our inversion method, and to identify the most relevant value of the regularization parameter λ, we calculate the RMS distance between the synthetic model (18) and the inverted models, as:

$$RMS = \sqrt{\frac{1}{N_f N_t} \sum_k \left[\mathbf{U}_i(t_k) - \mathbf{U}_s(t_k)\right]^T \left[\mathbf{U}_i(t_k) - \mathbf{U}_s(t_k)\right]}, \qquad (19)$$

where $\mathbf{U}_s$ and $\mathbf{U}_i$ are the synthetic and inverted slip vectors at time t_k (the synthetic slip is obtained using equation (18)). N_f and N_t are the number of nodes on the fault and the number of time steps considered. The RMS dependence on the regularization parameter λ and the number of gauges N_g is shown in Figure 6a, along with the minimum value of the objective function reached during the inversion iterations (L-curve) in Figure 6b. First, the RMS (Figure 6a) is essentially dependent on the number of strain gauges used in the inversion: it decreases roughly by a factor of ten when the number of strain gauges is increased by the same factor. Then, for a given configuration of strain gauges, the RMS is approximately constant for a wide range of λ values, and only increases at large λ. This latter tendency is also true for the objective function (Figure 6b), indicating the maximum value of λ one can use confidently without altering the fit to observations (and the RMS in the case of the synthetic test). As long as $\lambda \leq 10^{-2}$, it has a limited influence on the RMS (Figure 6a), and does not drastically modifies the performance of the inversion (Figure 6b). For the real strain gauge network ($N_g = 6$), when $\lambda \leq 10^{-2}$ the RMS is such that the synthetic model is retrieved with a typical error of $8\mu m$. For denser strain gauges, the RMS error could be reduced to 1μm, provided that the number of gauges is at least of the order of N_f (yellow, orange and green symbols in Figure 6a). For $\lambda > 10^{-2}$, the smoothing constrain becomes significant (Figure 6b), resulting in much higher values of the objective function. Based on the results of Figure 6, we therefore choose in the following $\lambda = 10^{-1}$ as the best compromise, since some smoothing is needed to balance the low resolution offered by the strain gauge array.

6 Application on injection experiments along existing frictional interface

We now apply the kinematic inversion procedure on the experimental results described in section 2, and shown in Figure 1b. Using this data set, we performed 3 kinematic inversions of fault slip, one for each red nucleation period shown in Figure 1b. In the main text, we develop the results obtained for Evt1 (between 700s and 1200s). The inversion results for the 2 other periods are provided in the supplementary material.

For each inversion, we proceeded in two steps. First we used the deterministic approach to obtain the model minimizing the objective function J given in equation (16). Then we used this result as an initial model in the probabilistic (MCMC) approach. We performed 2.10^6 steps for the MCMC algorithm, resulting in an acceptance rate between 0.2 and 0.32. The result of the second step is a posterior Probability Density Function for each parameter (each component of $\mathbf{X}$). The PDFs are presented in th esupplementary material (Figures S11 to S19). From these PDFs, we computed the best model $\bar{\mathbf{X}}$ (giving the maximum of the PDF) and the corresponding standard deviation on the model parameters σ_X, defined here as the 68^{th} percentile of the posterior parameter distribution. The results of the deterministic step for Evt1 are presented in Figures 7 and 8. Figures 9, 10 and 11 show the outcome of the MCMC step.

The best model resulting from the deterministic step (Figure 7) shows the nucleation of a first slip event on a small patch situated close to the injection site starting at about $t = 108$ s. This slipping patch remains localized, and slip reaches about 15 μm after about 300 s, which corresponds to a slip rate of $0.5\mu m.s^{-1}$, a typical value for slow aseismic slip. Between $t = 432$ s and $t = 486$ s a second slipping patch nucleates near $(x_1 = -1, x_2 = -1)$ (visible at $t = 486$ s). This latter event later expands in all directions, locally reaching 17 μm (last panel in Figure 7, $t = 648$ s). The expansion of the second slipping patch is typically of the order of a few centimeters in 100 s, that is 10 to 100 m per day. The propagation speed of the slip events observed in the experiment will be further discussed later (Figure 12).

The initiation of a first slip event close to the injection borehole is in agreement with what could be expected from mechanical arguments. The injection point is indeed the place where the pore pressure is the highest, so that it is the first place reaching the failure strength on the fault. For that reason, we believe that this first slipping patch is likely a robust feature, correctly imaged and located by the inversion. However, as shown from the restitution analysis (Figures 2b, c and d), the second slipping patch might result from a wrong attribution during the inversion process. Slip in the borehole region can for instance be assigned here (Figure 2b). We therefore think that this feature is not reliable, and would need to be confirmed with a denser gauge array. As shown in Figure 8, the inverted model provides a satisfactory fit to the strain and average slip measurements.

The MCMC step overall confirms the features revealed by the deterministic method, as illustrated in Figure 9: the initiation of a first crack at the injection borehole between $t = 107$ s and $t = 161$ s, followed by the nucleation of a second crack at time $t = 485$ s in the bottom left part of the fault, expanding until the end of the nucleation period. The initiation of the aseismic shear crack by the fluid injection is also visible in Figure

10: the maximum slip Δu (Figure 10a) shows a pattern roughly similar to the final slip distribution (final panel in Figure 9). Furthermore, the initiation time t_0 increases (Figure 10b) away from the slip initiation point (borehole). Interestingly the ramp duration T (rise time) is higher in the borehole region (1000 s) than on the remaining parts of the fault that has experienced slip (between 300 s and 700 s, Figure 10c).

The Bayesian approach also provides estimates of the parameters uncertainty (Figure 10d, e and f). The maximum uncertainties on Δu, t_0 and T reach about $5\mu m$, 40 s and 100 s respectively. Overall, the uncertainty on Δu, and t_0 is larger in the poorly resolved area defined from the resolution analysis (Figure 2a). This is however not the case for T. Nevertheless, we note that the posterior PDFs on model parameters can have a different shape depending on whether they characterize the well resolved or the poorly resolved areas (Figures S11, S12 and S13). As shown in the supplementary material, in the poorly resolved zone, the PDFs are often not Gaussian, exhibit multiple maxima, or can be close to a uniform distribution. In these cases, the standard deviation does not necessarily reflects the true uncertainty on the model parameters, which is better evaluated by visual inspection of the PDF itself.

Again, the models resulting from the Bayesian inversion provide a rather good fit to the measurements (Figure 11), comparable to the best model estimated in the deterministic approach. The models accepted during the MCMC iterations remain within the uncertainty on the measurements.

In order to assess the occurrence of propagating aseismic slip along the fault during Evt1, we present in Figure 12a how the onset time of slip t_0 changes with distance from the first node activated on the fault (initiation point of the slip event). To do that, we only considered the nodes situated in the well resolved area of the fault. The first node activated in this case is the node situated at $x_1 = 4cm, x_2 = 0$, close to the borehole. It is followed by the activation of a group of nodes from $t = 400$ s, situated more than 3 cm away from the first activated node. This group corresponds to the second slipping patch visible in Figures 7 and 9. To the first order, the time delay and the separation between the two slipping patches is consistent with an aseismic slip front propagating at about 10 m.day^{-1}. However, the resolution analysis has shown that the second slipping patch may be wrongly located. If instead we interpret this second patch as the expansion of the first slip event closer to the borehole (within the low resolution area for instance), this propagation speed would be increased by at least a factor 2. Furthermore, when looking at the dynamics of the second patch, the evolution of t_0 beyond 2 cm shown in Figure 12a suggests an expansion at a speed close to 100 m.day^{-1}. The expansion of aseismic slip during Evt2 and Evt3 shown in Figures 12b and c will be further discussed in the discussion section.

The results of this inversion and the synthetic tests conducted before, although affected by a very low resolution and possible artifacts, are to some extent promising. With a denser strain gauge array, our method could constrain the spatial and temporal evolution of the slip patch during the nucleation of our laboratory earthquakes.

7 Discussion: towards imaging fault slip during laboratory fault reactivation

In this work, we have tested a method to image centimetric scale aseismic quasi-static fault slip from local strain measurements in a tri-axial experimental setup, and to characterize the related uncertainty. With strain gauges distributed on one side of the fault, we are able to constrain slip front propagation only on one half of the fault plane. Using an even distribution of strain gauges (and possibly a higher number) would improve the resolution of the method. From the synthetic test, the best performance is obtained for a number of gauges larger or equal to the number of sub-fault used to infer fault slip. We have not investigated yet whether measuring other components of the strain tensor would improve the resolution. However the gauges used do not allow to measure two different components at the same position.

When applying this method to an injection experiment, we were able to identify some features of the nucleation process of a fluid induced stick-slip event. It consists of a shear crack initiated at the injection site, and expanding at a speed of the order of a few tens of m.day^{-1}. As shown in the supplementary material, we attempted to invert slip evolution during the nucleation of the 2 other stick-slip events (Evt2 and Evt3).

The inversion of Evt2 reveals once again the nucleation of an aseismic slip event in the region of the borehole, visible after about 80 s (Figures S1 and S5). As shown in Figure 12b, the slipping patch expands at a speed between 1 and 100 m.day^{-1}. We get again between $10\mu m$ and $17\mu m$ of maximum slip in the borehole region at the end of the observation period, implying again aseismic slip-rate. Note that the inverted model predicts strain and mean slip in overall agreement with the measurements, except for mean slip in the first 350s (Figures S2 and S7). This is the only case where observed average slip is decreasing towards negative values, which implies a reverse motion of the fault, a feature that is not allowed by our inversion method.

Finally Evt3 consists of the same kind of aseismic slip event as the one obtained in Evt1 and Evt2 (about $30\mu m$ of maximum slip after 1000 s, Figures S3 and S8). However, it nucleates at a different location, away from the borehole ($x_1 = -3.5$ cm, $x_2 =$ 0 cm). This could either be related to a wrong location during the inversion, but nucleation can also arise in this place because of the stress field left by the preceding stick slip events, possibly heterogeneous. To assess this latter hypothesis, we would need to perform the kinematic inversion for the dynamic (coseismic) phase of the stick-slip events, which requires the computation of elasto-dynamic Green's functions. This is beyond the scope of this study. The expansion of the aseismic slip patch occurs at a speed of approximately 10 m.day^{-1}, as suggested by the distribution of onset time with distance to the first node activated (Figure 12c).

More generally, since the nucleation of Evt2 and Evt3 might be affected by the preceding slip history on the fault, we decided to concentrate on the analysis of Evt1 in this study.

In the application presented here, we are not able yet to resolve differences in the propagation speeds of the different aseismic slip events imaged. Different propagation speeds could arise from the different mechanical conditions (stress, pore pressure) prevailing on the fault at the beginning of the nucleation process, or from the injection history. Increasing the coverage of the strain gauge array could eventually provide more information. Resolving such differences could largely improve our understanding of the mechanical control of aseismic slip propagation. Again, due to the uneven distribution of strain gauges, the inverse problem we tried to solve is slightly under-determined. This issue could probably be partly addressed by a different parametrization of fault slip, relying for instance on the elliptical sub-fault approximation used for earthquake source characterization (Vallée & Bouchon, 2004; Di Carli et al., 2010; Twardzik et al., 2014). This would however be a strong assumption about the slow slip pattern, and the method should be adapted to the specificities of aseismic slip, as derived from geodetical studies in subduction zones for instance (Radiguet et al., 2011b).

The slip front propagation speeds obtained here (of the order of 1 to 100 m.day^{-1}) can be compared to the aseismic slip front speeds observed on natural faults. Aseismic slip driving earthquake swarms or tremor bursts migrate at speeds between 100 m.day^{-1} and 10 km.day^{-1} (Lohman & McGuire, 2007; Obara, 2010; De Barros et al., 2020; Sirorattanakul et al., 2022). Slow slip events in subduction zones expand at speeds ranging from 100 m.day^{-1} to 10 km.day^{-1} (Radiguet et al., 2011b; Fukuda, 2018). Aftershocks are sometimes observed to migrate away from the main rupture, at speeds of several km per decade, a feature that is generally interpreted as resulting from the propagation of a postseismic aseismic slip front (Wesson, 1987; Peng & Zhao, 2009; Perfettini et al., 2019; Fan et al., 2022). The slower speeds observed in these experiments might be related to the particular setup (stress conditions or closeness to failure at the onset of slip), and to the injection rate. Initial stress and pressurization (injection) rates are indeed known to control the propagation speed of aseismic slip (Garagash & Germanovich, 2012; Dublanchet, 2019; Yang & Dunham, 2021). Our propagation speed of 10 m.day^{-1} is for instance within the range predicted by some models (Yang & Dunham, 2021).

The range of propagation speed estimated here during the nucleation phase is also several orders of magnitude smaller than the rupture speeds characterizing the stick slip events themselves (cm.s^{-1} to km.s^{-1}), as shown by Passelègue et al. (2020). The same experiment therefore generates a wide spectrum of fault slip events, from slow aseismic to dynamic ruptures. The kinematic inversion of fault slip presented here could be extended to image the dynamic rupture occurring during the stick-slip events. However, this would require to compute fully dynamic Green's functions instead of the static Green's function used here. This point is left for future investigation.

Slip events following the reactivation are likely triggered by the fluid injection. In Evt1 and Evt2, a slipping patch is indeed initiated at, or close to the injection site. Imaging the aseismic slip is thus interesting in a hydro-mechanical perspective. The inversion of pore pressure measurements performed for the same experiment by Almakari et al. (2020) shows that until stick slip event 3 (at $t = 3000$ s, Figure 1b), the hydraulic diffusivity within the fault D remains close to 1-2 m^2.s^{-1}. At $t = 3000$ s, the typical diffusion length $\sqrt{Dt}$ is about 5 to 6 cm, so that the entire fault is pressurized. The instantaneous fluid migration speed however is approximately $\sqrt{D/t} = 10^{-5}$ m.s^{-1}, an order of magnitude smaller than the aseismic slip migration speed. It is a typical feature predicted by hydro-mechanical models that on faults close enough to failure, aseismic slip propagation outpaces pore fluid pressure migration (Wynants-Morel et al., 2020; Dublanchet & De Barros, 2021). This feature has also been observed during decametric scale injection experiments triggering aseismic slip on a natural fault (Bhattacharya & Viesca, 2019). In order to better constrain the relationship between slip front and pressure front, further investigations are needed, either through new injection experiments with a denser strain gauge array, or by using fully coupled hydro-mechanical models to invert at the same time pore pressure, stress and slip measurements. The Green's function computed in this study could for instance be used in a mechanical model simulating fault slip evolution under specified frictional and hydraulic conditions, as developed in previous studies (Dublanchet & De Barros, 2021). This approach would also have the advantage of reducing the number of unknown parameters, since frictional properties could be determined separately.

Another possible application of the method developed here concerns the question of how aseismic moment scales with injected fluid volume V_f. The study of induced seismicity sequences suggests that seismic moment scales as V_f (McGarr, 2014), or as $V_f^{3/2}$ (Galis et al., 2017). Recent modeling studies have shown a scaling of the form $V_f^{3/2}$ for aseismic slip (Sáez et al., 2022). Imaging the development of aseismic slip during the controlled injection experiments will allow to provide more detailed insights into how this scaling can change through time. This objective is not yet achievable because of the limited resolution in our application. However this first experience provides insights on how to improve this issue in future application.

8 Conclusion

We have presented a kinematic inversion method to image aseismic slip on a centimetric scale laboratory fault loaded within a tri-axial setup. The forward model involves the computation of quasi-static Green's functions using finite elements analysis accounting for the cylindrical geometry of the rock sample, and the experimental loading conditions. After a series of synthetic tests allowing to better constrain the performance of the inversion method with respect to the configuration of the strain gauge array, we tested our method on a fault reactivation experiment involving a fluid injection. We showed that the injection triggers an aseismic slip event propagating at a speed of the order of 1 to 100 m.day^{-1} and leading to about $10-30$ μm of slip over a few hundreds of seconds before degenerating into a dynamic stick-slip event. This first attempt to image the dynamics of fault slip in the laboratory demonstrates the potential of strain inversion to better characterize earthquake nucleation process and hydro-mechanical fault behavior.

9 Open Research

To ensure full reproducibility and ease-of-use of our framework, we provide the data used to perform the inversions at (Dublanchet et al., 2023).

Acknowledgments

F.X.P acknowledges funding from the European Union (ERC Starting Grant HOPE num. 101041966).

References

Almakari, M., Chauris, H., Passelègue, F., Dublanchet, P., & Gesret, A. (2020). Fault's hydraulic diffusivity enhancement during injection induced fault reactivation: application of pore pressure diffusion inversions to laboratory injection experiments. *Geophysical Journal International*, *223*(3), 2117–2132.

Avouac, J.-P. (2015). From geodetic imaging of seismic and aseismic fault slip to dynamic modeling of the seismic cycle. *Annual Review of Earth and Planetary Sciences*, *43*(1), 233-271. doi: 10.1146/annurev-earth-060614-105302

Beresnev, I. A. (2003). Uncertainties in finite-fault slip inversions: To what extent to believe? (a critical review). *Bull. Seism. Soc. Am.*, *93*(6), 2445–2458. doi: 10.1785/0120020225

Bhattacharya, P., & Viesca, R. C. (2019). Fluid-induced aseismic fault slip outpaces pore-fluid migration. *Science*, *364*(6439), 464–468.

Bouchon, M. (1981). A simple method to calculate green's functions for elastic layered media. *Bulletin of the Seismological Society of America*, *71*(4), 959–971.

Bouchon, M., & Aki, K. (1977). Discrete wave-number representation of seismic-source wave fields. *Bulletin of the Seismological Society of America*, *67*(2), 259–277.

BRIAN, L. B. (1993). Fracture of brittle solids. *Cambridge solid state science series*, 307–334.

Broyden, C. G. (1970). The convergence of a class of double-rank minimization algorithms: 2. the new algorithm. *IMA journal of applied mathematics*, *6*(3), 222–231.

Cirella, A., Piatanesi, A., Cocco, M., Tinti, E., Scognamiglio, L., Michelini, A., ... Boschi, E. (2009). Rupture history of the 2009 l'aquila (italy) earthquake from non-linear joint inversion of strong motion and gps data. *Geophysical Research Letters*, *36*(19).

De Barros, L., Cappa, F., Deschamps, A., & Dublanchet, P. (2020). Imbricated aseismic slip and fluid diffusion drive a seismic swarm in the corinth gulf, greece. *Geophysical Research Letters*, *47*(9), e2020GL087142.

Di Carli, S., François-Holden, C., Peyrat, S., & Madariaga, R. (2010). Dynamic

intro.pdf

Figure 1. Experimental data set of stick-slip nucleation and description of the experimental setup and the forward problem a. Schematic view of the experimental fault system, and of the strain gauges array used in the inversion procedure. b. Evolution of the axial stress at each strain gauge location during the fluid injection along the fault interface (colors). The stress here is derived from the strain under a plane strain assumption. The red line indicates mean fault slip, the black line the injected pore pressure. The red time-windows correspond to the experimental data inverted using the kinematic model presented in c. Red vertical dotted lines and red stars indicate dynamic events. c. Schematic view of the fault system geometry and of the boundary conditions applied in the finite element simulations. The inset presents the evolution of the inelastic axial strain ε_{33} prior the first fluid-induced event (Evt1).

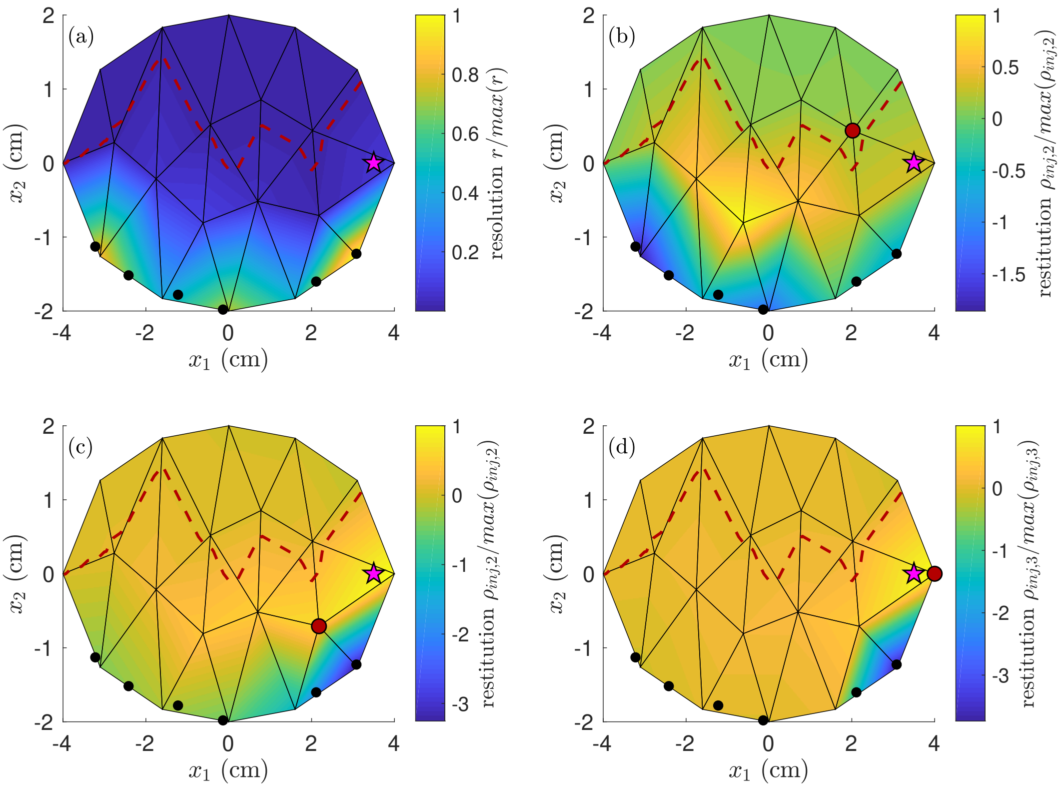

Figure 2. Resolution of the experimental array. (a) Diagonal elements r_i of the resolution matrix defined in equation (17), represented on the fault plane. The solid black lines indicate the mesh, and the black dots the experimental gauges array. The heavy red dashed line indicates a normalized resolution of 0.01. The magenta star indicates the injection borehole. (b), (c) and (d): Restitution $\rho_{inj,i}$ (off-diagonal elements of the resolution matrix) for three different nodes (red dots) close to the injection borehole.

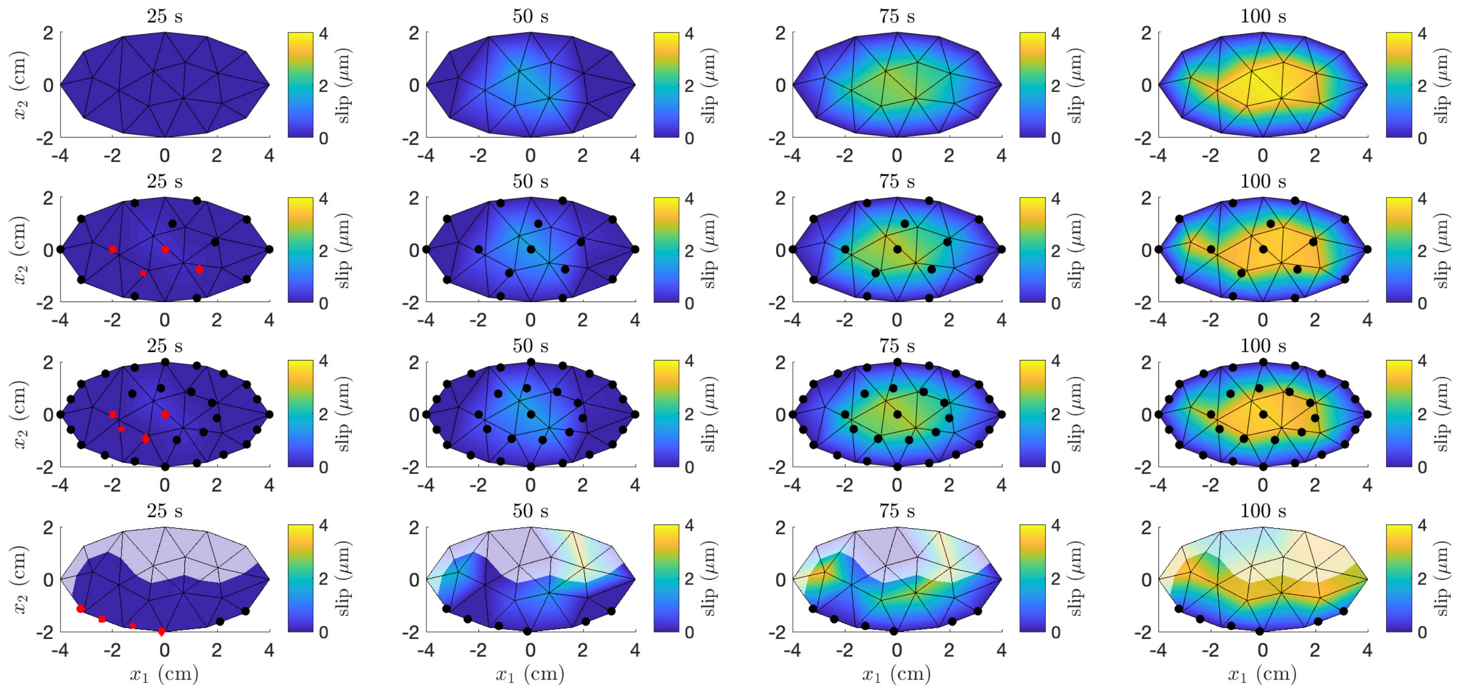

Figure 3. Synthetic test: fault slip distribution. Each panel is a top view of the fault, showing the fault slip distribution Δu (color-scale) at the time indicated in the title. The top row shows the true model to be retrieved, the others the inverted model with different strain gauges arrays. The triangular mesh used for the inversion is shown with solid black lines, and the projection of the strain gauges position is show with black dots. The second row corresponds to the result of a deterministic inversion with $N_g = 16$ gauges, the second row with $N_g = 31$ gauges, and the last row with the $N_g = 6$ gauges used in the real experimental setup (Figure 1a). The red symbols indicate the position of gauges G1 (dot), G2 (square), G3 (star) and G4 (diamond) mentioned in Figure 5. The transparent cache on the panels of the last row indicates a low resolution (below 0.01, see Figure 2 for details). The regularization parameter used here is $\lambda = 10^{-1}$.

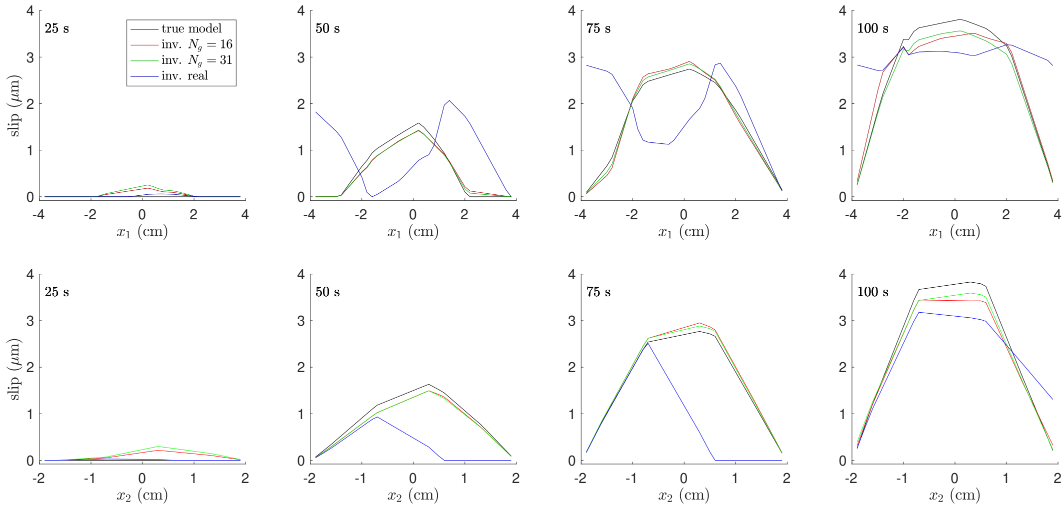

Figure 4. Synthetic test: slip profiles. The top row shows slip profiles along x_1, the second row along x_2, obtained from Figure 3 at different times. The true model to be retrieved (from equation (18)) is shown in black, inverted model predictions in red ($N_g = 16$), green ($N_g = 31$) and blue (experimental setup, $N_g = 6$).

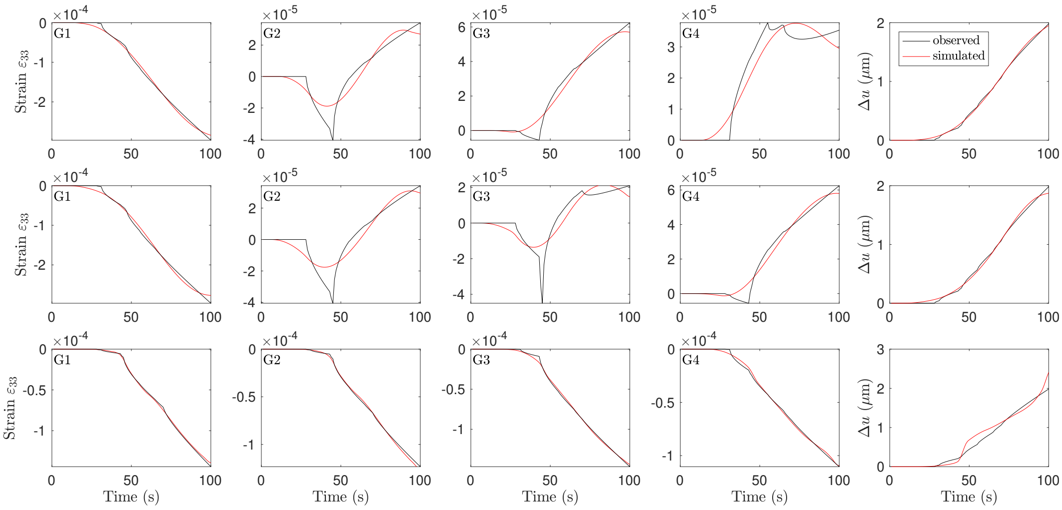

Figure 5. Synthetic test: observed and simulated strain and slip. Each row corresponds to one synthetic test performed with one gauge array (first row: $N_g = 16$, second row: $N_g = 31$ and last row: experimental setup, $N_g = 6$). Panels labeled G1, G2, G3 and G4 show the strain measured at the corresponding gauges (red symbols in Figure 3). The three right panels show the average slip. The black lines (observed) are the predictions of the true model, the red lines (simulated) are the predictions of the inverted models, shown in Figures 3 and 4.

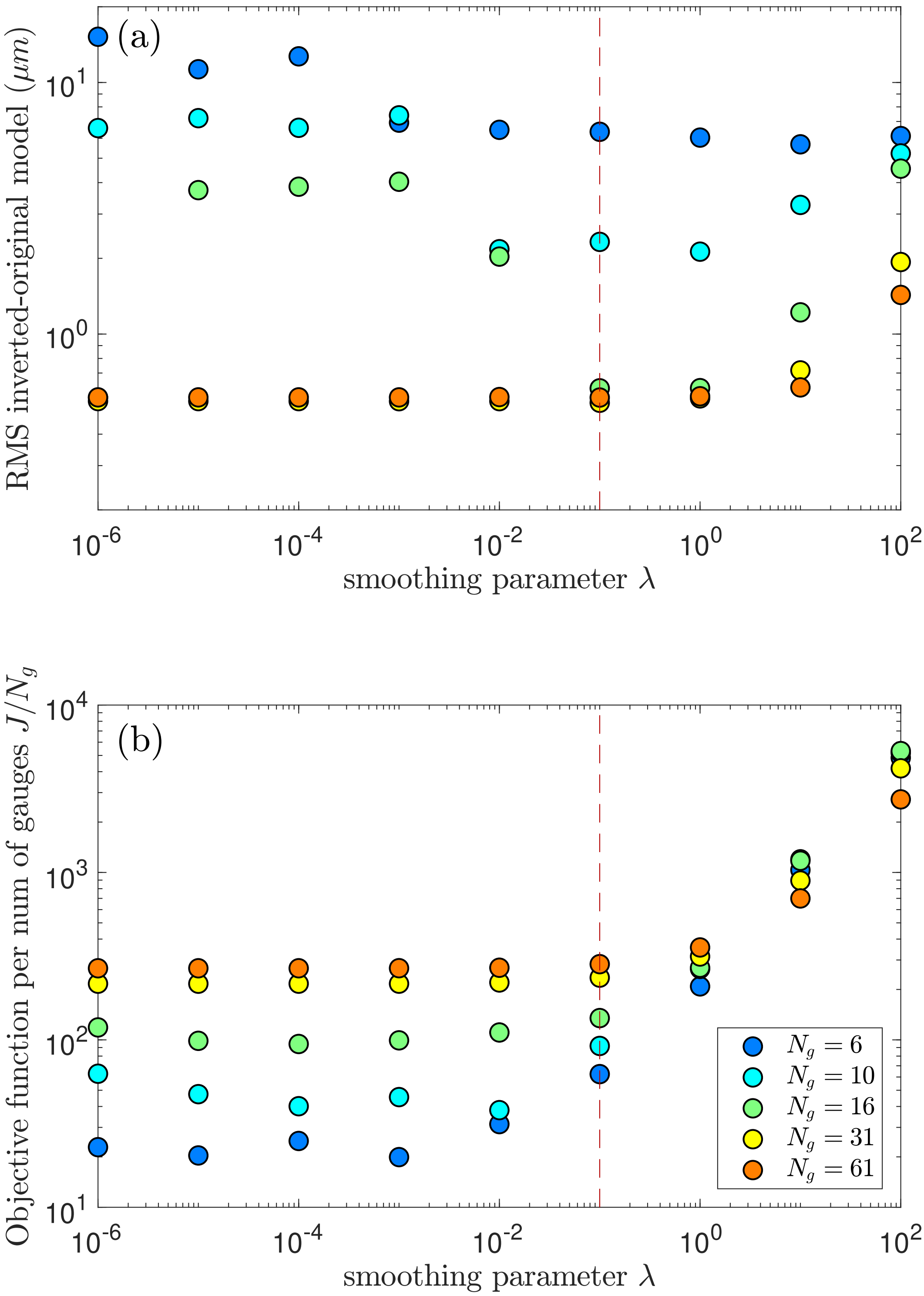

Figure 6. Synthetic tests summary. (a) RMS distance between true and inverted models. (b) Objective function per number of observations. The objective function is here the minimum value of J reached during the optimization, from equation (16). Colors refer to the strain gauge array. The red dashed vertical line indicates the optimal value of λ used in the inversion of the real experimental dataset.

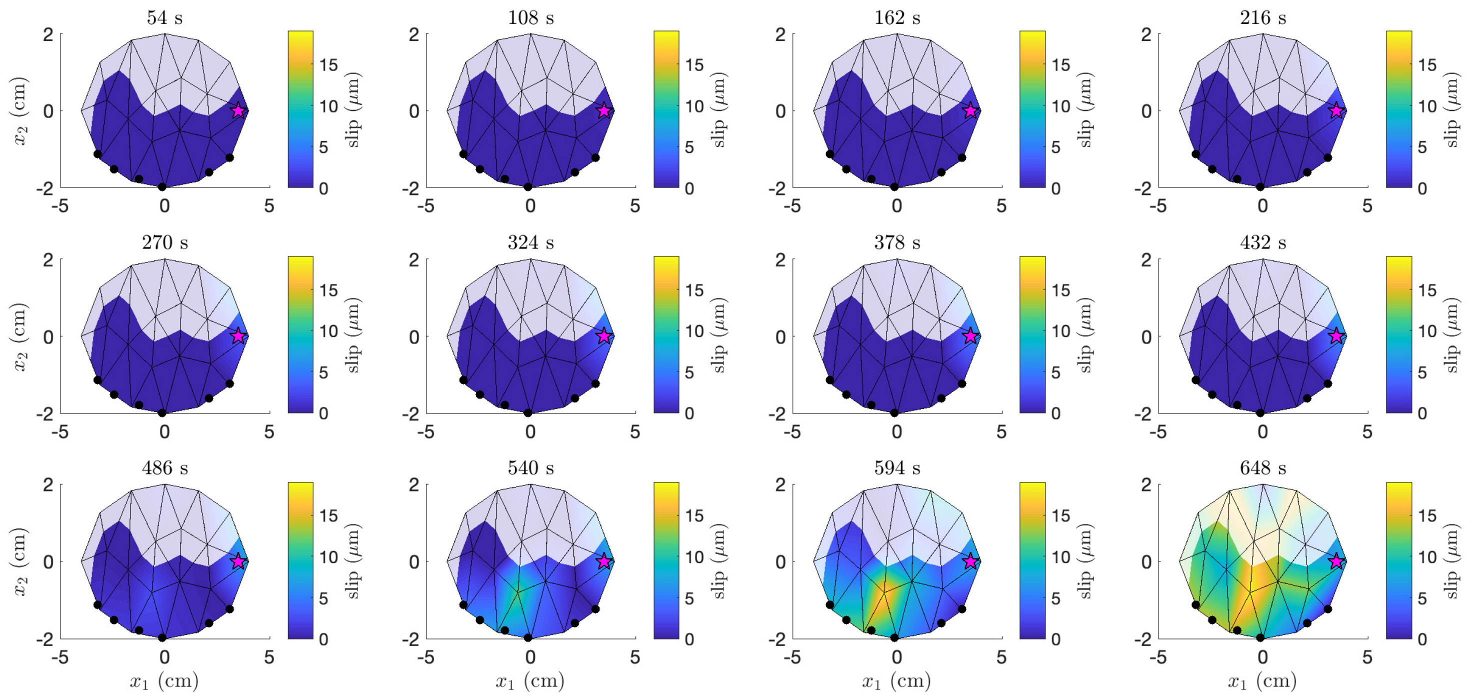

Figure 7. Kinematic inversion of Evt1 (nucleation phase), $\lambda = 10^{-1}$. Best model obtained from the deterministic inversion step. Each panel shows the inverted slip distribution at one time step indicated in the title. The mesh used for the inversion is shown as black solid lines and the experimental strain gauge array as black dots. The injection borehole position is indicated with the magenta star. The transparent cache indicates the low resolution area of the fault, as defined in Figure 2.

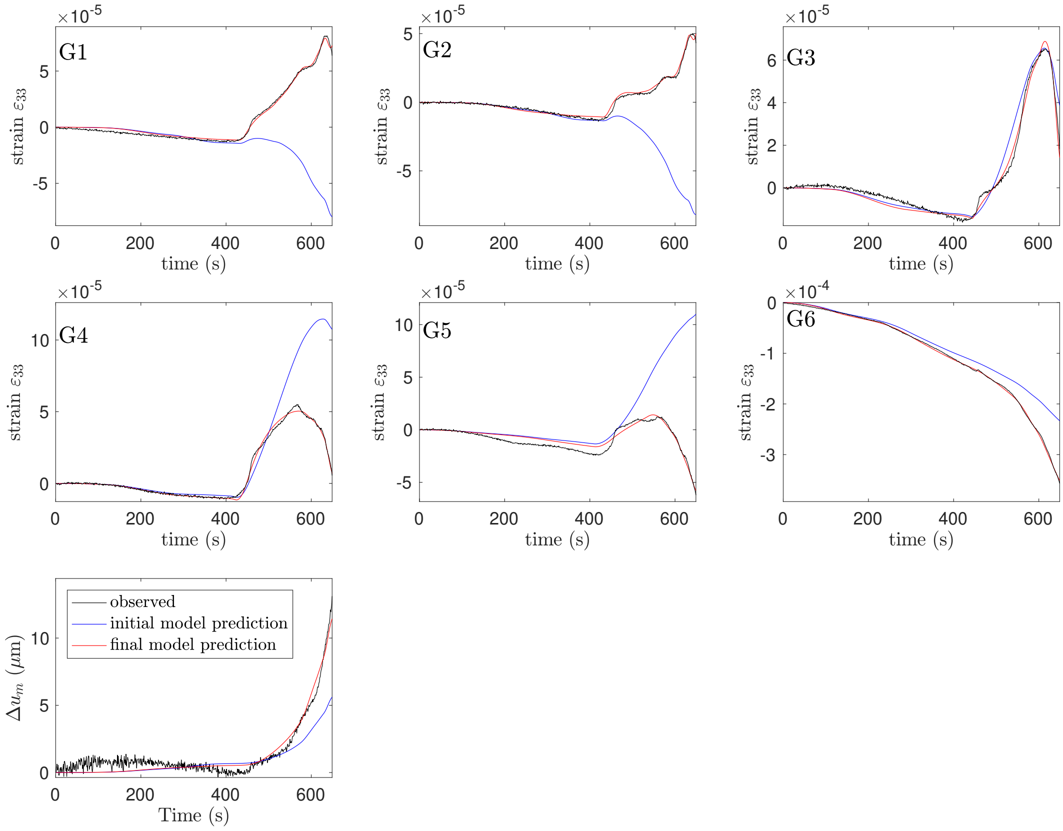

Figure 8. Observed (black) and modeled (red) strain and slip for Evt1. The model here is the outcome of the deterministic kinematic inversion of Evt1, shown in Figure 7. The strain gauges labeled G1 to G6, are sorted by increasing x_1 (left to right in Figure 7). The blue solid line indicates the prediction of the initial model used in the inversion.

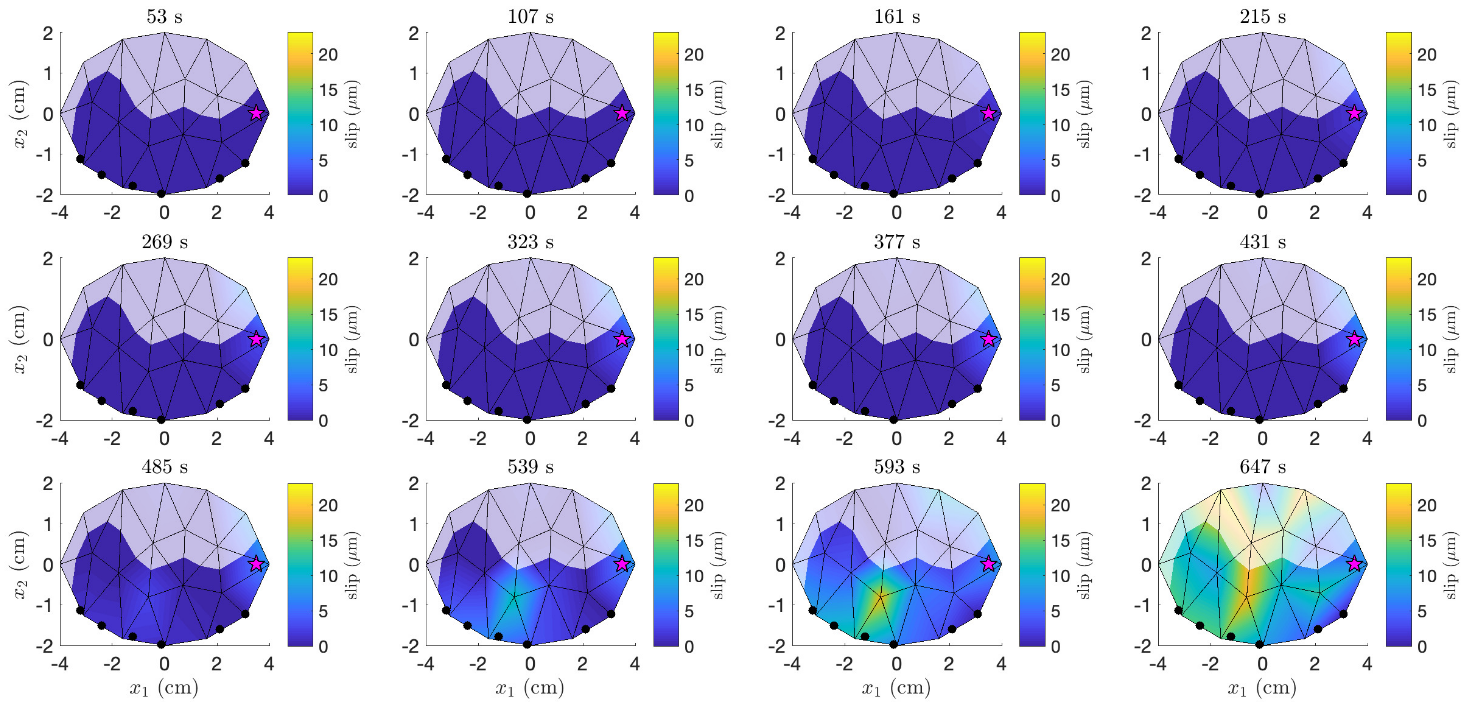

Figure 9. Kinematic inversion of Evt1. Best model obtained from the Bayesian inversion step (MCMC). See Figure 7 for details about the representation.

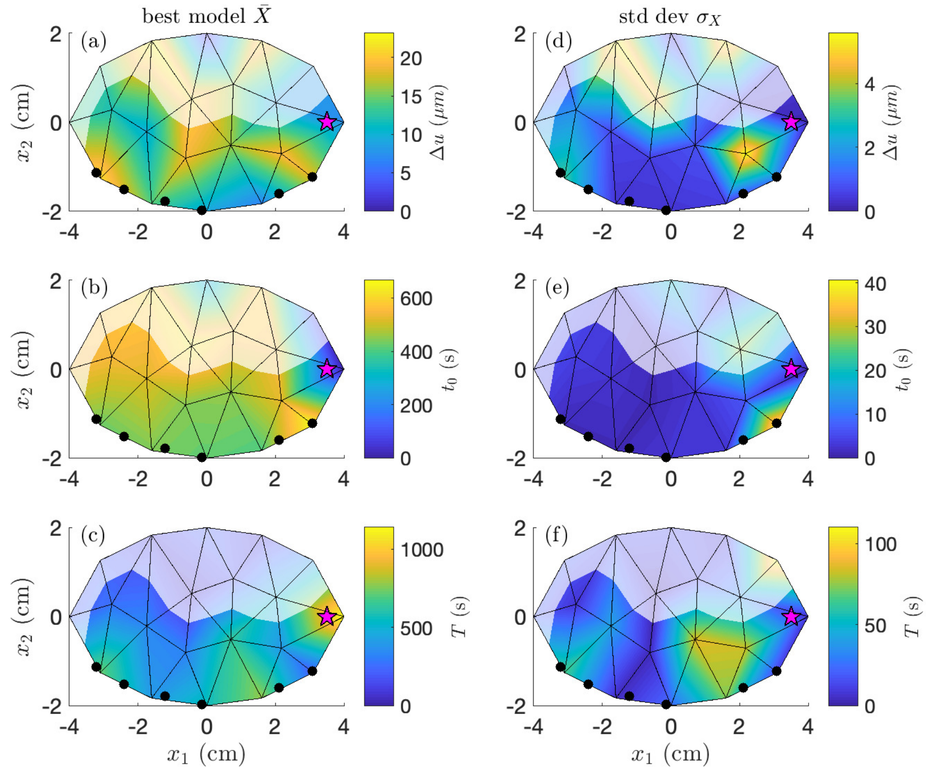

Figure 10. Kinematic inversion of Evt1. Best model parameters $\bar{\mathbf{X}}$ (left column) and standard deviation σ_X (right column) resulting from the Bayesian inversion step (MCMC). The best model parameters were used to construct the slip history shown in Figure 9. See Figure 9 for details about the representation.

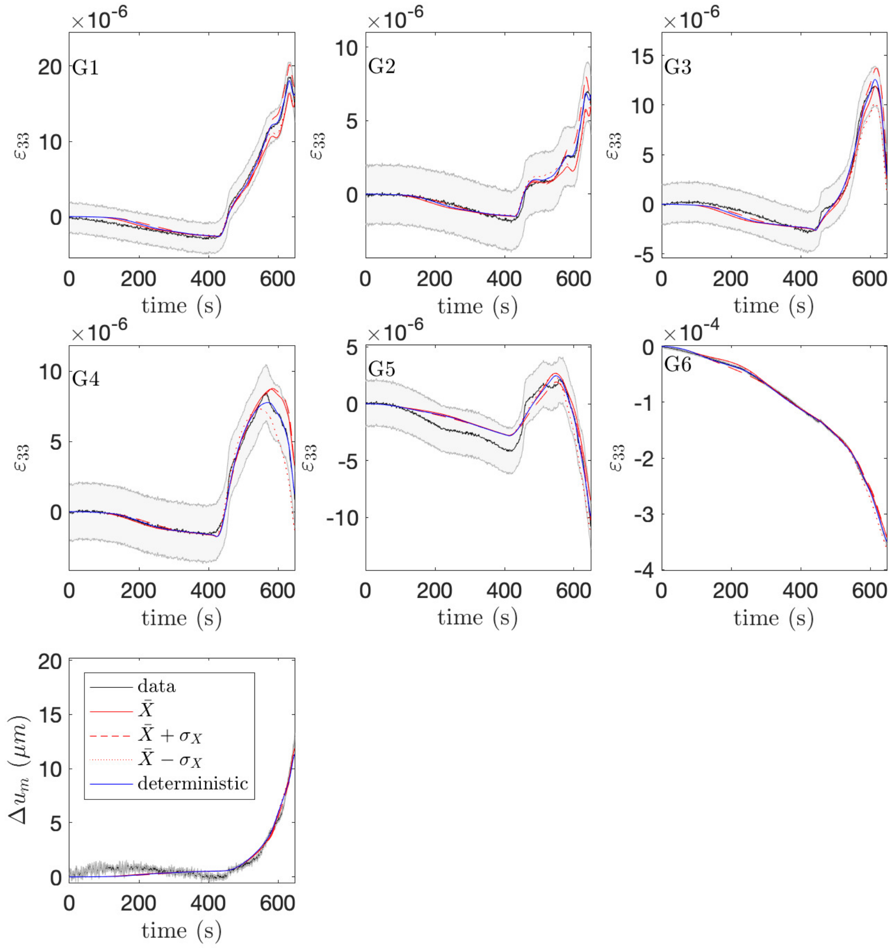

Figure 11. Observed (black) and modeled (red) strain and slip for Evt1. The models here are the outcome of the Bayesian kinematic inversion of Evt1, shown in Figures 9 and 10. The red solid line is the best model prediction, the dashed and dotted lines indicate the predictions of the models corresponding to the $\pm 1\sigma_X$ of the posterior distribution. The gray shaded zone indicates the experimental error on measurements, used to construct the covariance matrices.

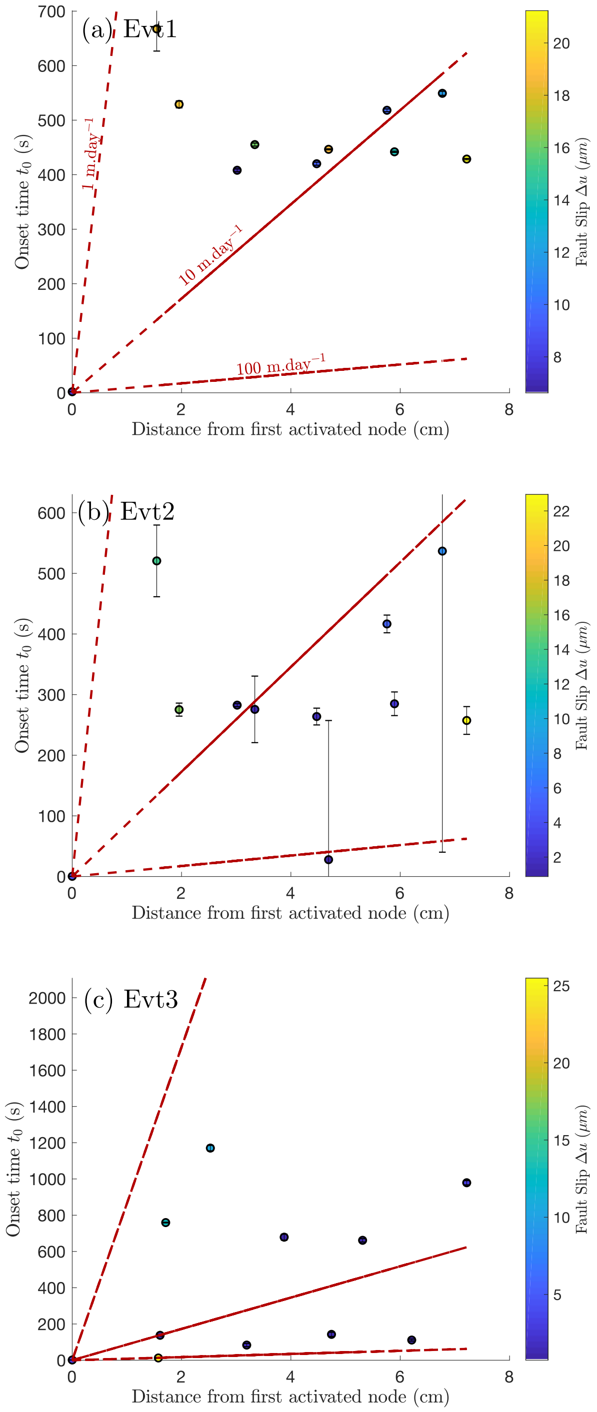

Figure 12. Onset time vs. distance to the first node activated for Evt1 (a), Evt2 (b) and Evt3 (c). The onset time is obtained from the Bayesian inversion. Each dot corresponds to one fault node. Only fault nodes situated in the well resolved area are represented here. The color indicates the inverted final slip Δu (Figure 10a). Errorbars are obtained from the posterior standard deviation presented in Figure 10d. The red dashed lines indicate propagation speeds of 1, 10 and 100 m.day^{-1}.

inversion of the 2000 tottori earthquake based on elliptical subfault approximations. *Journal of Geophysical Research: Solid Earth*, *115*(B12).

Dublanchet, P. (2019). Fluid driven shear cracks on a strengthening rate-and-state frictional fault. *Journal of the Mechanics and Physics of Solids*, *132*, 103672.

Dublanchet, P., & De Barros, L. (2021). Dual seismic migration velocities in seismic swarms. *Geophysical Research Letters*, *48*(1), e2020GL090025.

Dublanchet, P., Passelègue, F. X., Chauris, H., Gesret, A., & Twardzik, C. (2023, June). *Strain and slip data for Kinematic inversion of fault slip during the nucleation of laboratory earthquakes.* Zenodo. Retrieved from `https://doi.org/10.5281/zenodo.8081719` doi: 10.5281/zenodo.8081719

Fan, L., Li, B., Liao, S., Jiang, C., & Fang, L. (2022). Precise earthquake sequence relocation of the january 8, 2022, qinghai menyuan ms6. 9 earthquake. *Earthq. Sci.*, *35*, 138–145.

Fletcher, R. (1970). A new approach to variable metric algorithms. *The computer journal*, *13*(3), 317–322.

Fletcher, R. (1982). A model algorithm for composite nondifferentiable optimization problems. *Nondifferential and Variational Techniques in Optimization*, 67–76.

Fukuda, J. (2018). Variability of the space-time evolution of slow slip events off the boso peninsula, central japan, from 1996 to 2014. *Journal of Geophysical Research: Solid Earth*, *123*(1), 732–760.

Galis, M., Ampuero, J. P., Mai, P. M., & Cappa, F. (2017). Induced seismicity provides insight into why earthquake ruptures stop. *Science advances*, *3*(12), eaap7528.

Gallovič, F., & Zahradník, J. (2012). Complexity of the mw 6.3 2009 l'aquila (central italy) earthquake: 1. multiple finite-extent source inversion. *Journal of Geophysical Research: Solid Earth*, *117*(B4).

Garagash, D. I., & Germanovich, L. N. (2012). Nucleation and arrest of dynamic slip on a pressurized fault. *Journal of Geophysical Research: Solid Earth*, *117*(B10).

Goldfarb, D. (1970). A family of variable-metric methods derived by variational means. *Mathematics of computation*, *24*(109), 23–26.

Goto, S., Tatsuoka, F., Shibuya, S., Kim, Y., & Sato, T. (1991). A simple gauge for local small strain measurements in the laboratory. *Soils and foundations*, *31*(1), 169–180.

Hartzell, S., Liu, P., Mendoza, C., Ji, C., & Larson, K. M. (2007). Stability and uncertainty of finite-fault slip inversions: Application to the 2004 parkfield, california, earthquake. *Bull. Seism. Soc. Am.*, *97*(6), 1911–1934. doi: 10.1785/0120070080

Hartzell, S. H., & Heaton, T. H. (1983). Inversion of strong ground motion and teleseismic waveform data for the fault rupture history of the 1979 imperial valley, california, earthquake. *Bulletin of the Seismological Society of America*, *73*(6A), 1553-1583. doi: 10.1785/BSSA07306A1553

Hastings, W. K. (1970). Monte carlo sampling methods using markov chains and their applications.

Ide, S. (2007). *4.07 - slip inversion* (G. Schubert, Ed.). Amsterdam: Elsevier. doi: 10.1016/B978-044452748-6.00068-7

Ji, C., Wald, D. J., & Helmberger, D. V. (2002). Source description of the 1999 hector mine, california, earthquake, part i: Wavelet domain inversion theory and resolution analysis. *Bulletin of the Seismological Society of America*, *92*(4), 1192-1207. doi: 10.1785/0120000916

Johnson, K. M., Fukuda, J., & Segall, P. (2012). Challenging the rate-state asperity model: Afterslip following the 2011 m9 tohoku-oki, japan, earthquake. *Geophysical Research Letters*, *39*(20).

Johnson, L. R. (1974). Green's function for lamb's problem. *Geophysical Journal International*, *37*(1), 99–131.

Lamb, H. (1904). I. on the propagation of tremors over the surface of an elastic solid. *Philosophical Transactions of the Royal Society of London. Series A, Containing papers of a mathematical or physical character*, *203*(359-371), 1–42.

Liu, P., Custódio, S., & Archuleta, R. J. (2006). Kinematic inversion of the 2004 m 6.0 parkfield earthquake including an approximation to site effects. *Bulletin of the Seismological Society of America*, *96*(4B), S143–S158.

Lockner, D., Byerlee, J., Kuksenko, V., Ponomarev, A., & Sidorin, A. (1992). Observations of quasistatic fault growth from acoustic emissions. In *International geophysics* (Vol. 51, pp. 3–31). Elsevier.

Lohman, R., & McGuire, J. (2007). Earthquake swarms driven by aseismic creep in the salton trough, california. *Journal of Geophysical Research: Solid Earth*, *112*(B4).

Mai, P. M., Schorlemmer, D., Page, M., Ampuero, J., Asano, K., Causse, M., . . . Zielke, O. (2016). The earthquake-source inversion validation (siv) project. *Seismological Research Letters*, *87*(3), 690-708. doi: 10.1785/0220150231

McGarr, A. (2014). Maximum magnitude earthquakes induced by fluid injection. *Journal of Geophysical Research: solid earth*, *119*(2), 1008–1019.

Metropolis, N., Rosenbluth, A. W., Rosenbluth, M. N., Teller, A. H., & Teller, E. (1953). Equation of state calculations by fast computing machines. *The journal of chemical physics*, *21*(6), 1087–1092.

Obara, K. (2010). Phenomenology of deep slow earthquake family in southwest japan: Spatiotemporal characteristics and segmentation. *Journal of Geophysical Research: Solid Earth*, *115*(B8).

Olson, A. H., & Apsel, R. J. (1982). Finite faults and inverse theory with applications to the 1979 imperial valley earthquake. *Bulletin of the Seismological Society of America*, *72*(6A), 1969-2001. doi: 10.1785/BSSA07206A1969

Passelègue, F. X., Almakari, M., Dublanchet, P., Barras, F., Fortin, J., & Violay, M. (2020). Initial effective stress controls the nature of earthquakes. *Nature communications*, *11*(1), 5132.

Passelègue, F. X., Aubry, J., Nicolas, A., Fondriest, M., Deldicque, D., Schubnel, A., & Di Toro, G. (2019). From fault creep to slow and fast earthquakes in carbonates. *Geology*, *47*(8), 744–748.

Passelègue, F. X., Schubnel, A., Nielsen, S., Bhat, H. S., Deldicque, D., & Madariaga, R. (2016). Dynamic rupture processes inferred from laboratory microearthquakes. *Journal of Geophysical Research: Solid Earth*, *121*(6), 4343–4365.

Peng, Z., & Zhao, P. (2009). Migration of early aftershocks following the 2004 parkfield earthquake. *Nature Geoscience*, *2*(12), 877–881.

Perfettini, H., Frank, W., Marsan, D., & Bouchon, M. (2019). Updip and along-strike aftershock migration model driven by afterslip: Application to the 2011 tohoku-oki aftershock sequence. *Journal of Geophysical Research: Solid Earth*, *124*(3), 2653–2669.

Peyrat, S., & Olsen, K. (2004). Nonlinear dynamic rupture inversion of the 2000 western tottori, japan, earthquake. *Geophysical research letters*, *31*(5).

Radiguet, M., Cotton, F., Vergnolle, M., Campillo, M., Valette, B., Kostoglodov, V., & Cotte, N. (2011a). Spatial and temporal evolution of a long term slow slip event: the 2006 guerrero slow slip event. *Geophysical Journal International*, *184*(2), 816–828.

Radiguet, M., Cotton, F., Vergnolle, M., Campillo, M., Valette, B., Kostoglodov, V., & Cotte, N. (2011b). Spatial and temporal evolution of a long term slow slip event: the 2006 guerrero slow slip event. *Geophysical Journal International*, *184*(2), 816–828.

Sáez, A., Lecampion, B., Bhattacharya, P., & Viesca, R. C. (2022). Three-dimensional fluid-driven stable frictional ruptures. *Journal of the Mechanics* *and Physics of Solids*, *160*, 104754.

Saraó, A., Das, S., & Suhadolc, P. (1998). Effect of non-uniform station coverage on the inversion for earthquake rupture history for a haskell-type source model. *Journal of Seismology*, *2*, 1-25. doi: 10.1023/A:1009795916726

Shanno, D. F. (1970). Conditioning of quasi-newton methods for function minimization. *Mathematics of computation*, *24*(111), 647–656.

Sirorattanakul, K., Ross, Z. E., Khoshmanesh, M., Cochran, E. S., Acosta, M., & Avouac, J.-P. (2022). The 2020 westmorland, california earthquake swarm as aftershocks of a slow slip event sustained by fluid flow. *Journal of Geophysical Research: Solid Earth*, *127*(11), e2022JB024693.

Tarantola, A. (2005). *Inverse problem theory and methods for model parameter estimation.* SIAM.

Twardzik, C., Das, S., & Madariaga, R. (2014). Inversion for the physical parameters that control the source dynamics of the 2004 parkfield earthquake. *Journal of Geophysical Research: Solid Earth*, *119*(9), 7010–7027.

Twardzik, C., Duputel, Z., Jolivet, R., Klein, E., & Rebischung, P. (2022). Bayesian inference on the initiation phase of the 2014 iquique, chile, earthquake. *Earth and Planetary Science Letters*, *600*, 117835.

Twardzik, C., Vergnolle, M., Sladen, A., & Tsang, L. L. (2021). Very early identification of a bimodal frictional behavior during the post-seismic phase of the 2015 m w 8.3 illapel, chile, earthquake. *Solid Earth*, *12*(11), 2523–2537.

Vallée, M., & Bouchon, M. (2004). Imaging coseismic rupture in far field by slip patches. *Geophysical Journal International*, *156*(3), 615–630.

Vallée, M., Xie, Y., Grandin, R., Villegas-Lanza, J. C., Nocquet, J.-M., Vaca, S., ... others (2023). Self-reactivated rupture during the 2019 mw= 8 northern peru intraslab earthquake. *Earth and Planetary Science Letters*, *601*, 117886.

Wesson, R. L. (1987). Modeling aftershock migration and afterslip of the san juan bautista, california, earthquake of october 3, 1972. *Tectonophysics*, *144*(1-3), 215–229.

Wynants-Morel, N., Cappa, F., De Barros, L., & Ampuero, J.-P. (2020). Stress perturbation from aseismic slip drives the seismic front during fluid injection in a permeable fault. *Journal of Geophysical Research: Solid Earth*, *125*(7), e2019JB019179.

Yang, Y., & Dunham, E. M. (2021). Effect of porosity and permeability evolution on injection-induced aseismic slip. *Journal of Geophysical Research: Solid Earth*, *126*(7), e2020JB021258.